

Momentum-resolved detection for high-precision Bragg atom interferometry

Yuan Cheng, Ke Zhang, Le-Le Chen, Tao Zhang, Wen-Jie Xu, Xiao-Chun Duan, Min-Kang Zhou,^{*} and Zhong-Kun Hu[†]
 MOE Key Laboratory of Fundamental Physical Quantities Measurements, Hubei Key Laboratory of Gravitation and Quantum Physics,
 School of Physics, Huazhong University of Science and Technology, Wuhan 430074, People's Republic of China



(Received 20 May 2018; revised manuscript received 5 September 2018; published 9 October 2018)

We demonstrate a momentum-resolved detection technique in a sensitive Bragg atom interferometer, where the populations of the atomic final states are measured by the Raman spectroscopy method. This method avoids cross-couplings due to the space overlapping of atomic states and significantly increases the fringe visibility without requiring spatial separation. Thanks to this detection method, we are able to achieve the high fringe visibility of greater than 80% at an interrogation time of $T = 1$ ms. With $T = 250$ ms and a visibility of 10%, it shows an improved resolution for gravity measurements at the level of $7 \times 10^{-10} g$ in an integration time of 1000 s. This work can be applied in developing compact portable sensing devices or improving the precision of tests on fundamental physics.

DOI: [10.1103/PhysRevA.98.043611](https://doi.org/10.1103/PhysRevA.98.043611)

I. INTRODUCTION

The cold-atom interferometer has achieved outstanding performance for high-precision measurements, such as measurements of gravity [1–3] and its gradients [4], the Sagnac effect [5], the fine-structure constant α [6], Newton's gravitational constant G [7], the magnetic field [8], and tests of fundamental physics [9–13]. For such interferometers, measurement of the populations in each final state was achieved with low-noise atom detection methods. Standard detection strategies for atomic final-state detection include measuring scattered fluorescence [14] or optical absorption [15,16], whose signal-to-noise ratio (SNR) can be as high as several hundreds or even better. Based on these two detection strategies, there are many implementations for different experimental apparatuses, such as two-state sequential detection [17], two-state simultaneous detection [18], frequency modulation imaging [19], and Raman spectroscopy (RS) imaging [20,21]. Each individual detection technique is best suited for a particular system. Recently, Bragg atom interferometers have received more and more attention due to their property of multiphoton momentum transfer and unchanged internal atomic states [22–25]. However, the accompanying problem is that the interferometer's output ports cannot be separated enough in space to identify them independently, due to the thermal expansion of the atomic cloud and the short flight time before arriving at the detection region [26,27]. More important, because Bragg transitions usually couple multiple momentum states, an impure detection also induces a multistate Bragg interferometer and results in systematic phase shifts [24,28]. Therefore, a suitable detection technique is essential in a high-precision Bragg atom interferometer. As we know, coupling atomic ground states with counter-propagating laser beams in

Raman transitions is very efficient and can happen in a narrow atom velocity distribution that meets the resonant condition. Thus, the interferometer's output states at different velocities can be imaged in RS by scanning the frequency difference of Raman beams.

In this paper, we perform a momentum-resolved detection scheme based on RS for the Bragg atom gravimeter. This scheme measures the atomic momentum distribution in the frequency domain and completely identifies the overlapped atomic cloud in momentum space without requiring an extremely long flight time. To simplify practical experiments, we propose and demonstrate a compact and robust laser system used to perform both Bragg and Raman transitions with a single laser source. Compared with time-of-flight (TOF) detection, RS detection greatly improves the fringe visibility, especially at long interrogation times $2T$, allowing a high fringe visibility, greater than 80%, to be observed. In particular, we explore the effect of the Raman pulse duration on the fringe contrast, and the experimental results are in agreement with the theoretical model. Finally, we demonstrate a high-sensitivity Bragg atom interferometer based on the RS detection method, which achieves a short-term sensitivity of $1.9 \times 10^{-8} g/\sqrt{\text{Hz}}$ for gravity measurements.

II. THEORY

In n th-order Bragg diffraction, the atom coherently scatters $2n$ photons from a pair of counterpropagating laser beams, without changing its internal state. The atom thereby acquires a momentum of $2n\hbar k$, where $\hbar k$ is the photon momentum. If n th-order Bragg diffraction acts as atom-optic beam splitters ($\pi/2$ pulses) and mirrors (π pulses) in the Mach-Zehnder ($\pi/2$ - π - $\pi/2$) configuration, the mean transition probability P_n to the final state $|p - 2n\hbar k\rangle$ is determined by the interference phase shift $\Delta\Phi$ as $P_n = [1 + C \cos(\Delta\Phi)]/2$, where C is the contrast of the interferometry fringe. The normalized transition probability P_n is given by $P_n = N_{p-2n\hbar k} / (N_{p-2n\hbar k} + N_p)$, where N_p and $N_{p-2n\hbar k}$ denote the atomic

^{*}zmk@hust.edu.cn

[†]zkhu@hust.edu.cn

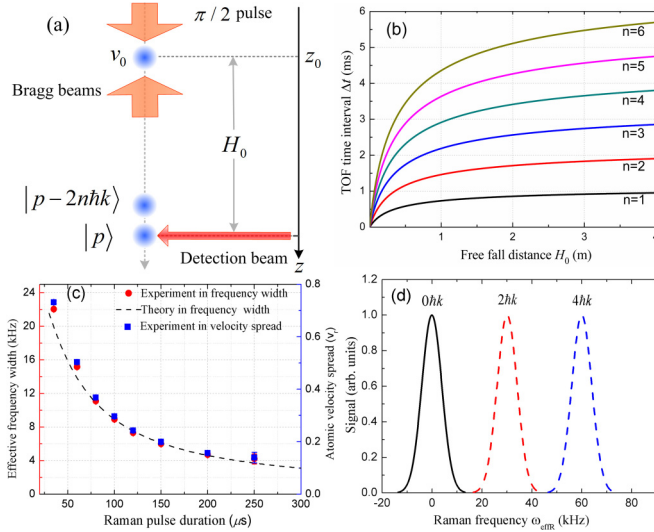


FIG. 1. (a) TOF detection scheme for the Bragg atom interferometer. (b) Expected time interval Δt for atoms in different momentum states as a function of the atomic free fall distance between moments of the final $\pi/2$ pulse and the atoms reaching the center of the detection region. Here, the initial velocity of the atoms at the moment of the final $\pi/2$ pulse is $v_0 = 1.88$ m/s. With a typical free-fall height of $H_0 = 0.3$ m, the interferometer's output states with low-order diffraction ($n \leq 5$) are not sufficiently separated before being detected. (c) Atomic velocity spread and its corresponding effective frequency width, as a function of the Raman-pulse duration. The dashed line represents the theoretical calculation, which is a good fit for the experimental results (red circles). (d) Theoretical RS of atoms under quasi-Bragg diffraction. The detecting Raman pulse duration is $100 \mu s$ in the simulation. The three signals (black, dashed red, and dashed blue lines) indicate the atomic momentum distribution in the frequency domain, which includes the $0\hbar k$, $2\hbar k$, and $4\hbar k$ outputs, respectively.

population of the interferometer's output states $|p\rangle$ and $|p - 2n\hbar k\rangle$, respectively. They can be directly detected in the form of TOF signal by photodetectors [26,29] and can be expressed as

$$N_p = \int_{-\infty}^{\infty} V_p(t) dt, \quad (1)$$

$$N_{p-2n\hbar k} = \int_{-\infty}^{\infty} V_{p-2n\hbar k}(t + \Delta t) dt.$$

$V_p(t)$ and $V_{p-2n\hbar k}(t)$ are the detected TOF signals for the $|p\rangle$ and $|p - 2n\hbar k\rangle$ momentum states, respectively, and Δt is the time interval between the $|p\rangle$ and the $|p - 2n\hbar k\rangle$ momentum states arriving at the center of the detection region from the final $\pi/2$ pulse. Figure 1(a) shows the TOF detection scheme of our experimental apparatus. Once the final $\pi/2$ pulse is completed, atoms with different momentum states begin to separate in space until they reach the detection region. When the atoms reach the center of the detection region with a free-fall height of H_0 between the last interferometer pulse and the center of the detection region, the equation of motion can be written as

$$H_0 = (v_0 - 2nv_r)t_n + \frac{1}{2}gt_n^2, \quad (2)$$

where v_0 is the initial velocity of the atoms at the moment of the final $\pi/2$ pulse, and t_n is the mean flight time for the $|p - 2n\hbar k\rangle$ momentum state with a free-fall height of H_0 . By solving Eq. (2), t_n can be written as

$$t_n = \frac{-v_0 + 2nv_r + \sqrt{2gH_0 + (v_0 - 2nv_r)^2}}{g}. \quad (3)$$

Then the time interval Δt can be calculated as $\Delta t = t_n - t_0$ and developed further as

$$\Delta t = \frac{\sqrt{2gH_0 + (v_0 - 2nv_r)^2} - \sqrt{2gH_0 + v_0^2} + 2nv_r}{g}. \quad (4)$$

For a high initial velocity v_0 compared to the recoil velocity of multiphotons ($v_0 \gg 2nv_r$), Eq. (4) can be rewritten as

$$\Delta t = \frac{2nv_r}{g}. \quad (5)$$

There is a limit to the time interval Δt , which is proportional to Bragg orders n . In other words, if the two output states need to be clearly identified in the TOF signal, their diffraction order must be high enough. Moreover, for a compact interferometer, the available free-fall distance for spatial separation is also limited.

In our apparatus, the atomic source is launched to a height of 0.66 m above the magneto-optical trap (MOT) center, the center of the detection region is 0.18 m above the MOT center, and the $1/e^2$ Gaussian width of the falling TOF signal is $w = 2.3$ ms. The initial velocity of the atoms at the moment of the final $\pi/2$ pulse is $v_0 = 1.88$ m/s. The two output states of the interferometer can be spatially identified only when their time interval is set to $\Delta t \geq 2w$. Figure 1(b) shows the expected time interval Δt as a function of the atomic free-fall distance H_0 for a variety of Bragg orders n , according to Eq. (4). With a typical free-fall height of $H_0 = 0.3$ m, the interferometer's output states with low-order diffraction ($n \leq 5$) are not sufficiently separated before being detected. Specifically, if the two output states ($n = 0$ and $n = 5$) in a fifth-order Bragg atom interferometer need to be clearly identified, then an extra flying distance of 3 m is required. Obviously, this will further enlarge the whole vacuum chamber and is inadvisable, especially for a compact quantum sensor. But if we employ the RS method, the problem of requiring a long flight time will no longer exist because RS is sensitive to the momentum of atoms and is able to clearly identify the population of the wave packet in frequency domain.

The RS method is based on two-photon-stimulated Raman transitions [30], which are usually used to coherently manipulate atomic wave packets in the atom interferometer. In our apparatus, a prevelocity selection Raman pulse is applied to atoms in the state preparation stage, which ensures that the width of the atoms' velocity spread in the vertical direction is smaller than the recoil velocity v_r . As shown in Fig. 1(c), the width of the velocity spread σ_v is about $0.3v_r$ (30 kHz) in the case of a Raman pulse duration of $100 \mu s$. When the atoms fall back to the detection chamber, Raman beams are used again to measure the atomic momentum distribution in the frequency domain. For a typical three-level system, we

define the detuning δ for two-photon transitions as

$$\delta = \omega_{\text{effR}} - \left(\omega_{ba} + \frac{pk_{\text{effR}}}{m} + \frac{\hbar k_{\text{effR}}^2}{2m} \right), \quad (6)$$

where the effective laser frequency ω_{effR} is defined as $\omega_{\text{effR}} = \omega_{L1} - \omega_{L2}$, ω_{L1} and ω_{L2} are the frequencies of two counter-propagating Raman beams, the effective wave vector k_{effR} of Raman beams is defined as $k_{\text{effR}} = k_{L1} + k_{L2} \approx 2k$, k_{L1} and k_{L2} are the wave vectors of two counter-propagating Raman beams, pk_{effR}/m is the Doppler shift, and $\hbar k_{\text{effR}}^2/2m$ is the recoil shift. A Doppler-sensitive configuration with counter-propagating Raman beams is chosen for velocity selection. Atoms with a certain velocity component parallel to the Raman beams will be exactly in resonance when the Doppler shift compensates the detuning. Theoretical calculations of the velocity selection with different pulse durations have been performed [27,31]. In our experiments, the theoretical curve (dashed curve) is a good fit for the experimental results (red points) as shown in Fig. 1(c). We find that the effective frequency width ($1/e^2$ Gaussian width) of the Raman transitions can reach a few kilohertz with long-pulse durations, which is a key component for identifying atomic momentum states in RS.

In quasi-Bragg diffraction [32], the adjacent momentum states have a momentum difference of $\Delta p = 2\hbar k$, corresponding to a frequency difference in RS detection of

$$\Delta\omega_{\text{effR}} = k_{\text{effR}} v_r, \quad (7)$$

where $v_r \approx 5.9$ mm/s is the single-photon recoil velocity on the ^{87}Rb D_2 line, and the corresponding frequency interval of the adjacent momentum states is calculated to be $\Delta\omega_{\text{effR}} = 2\pi \times 30.1$ kHz. In fact, the width of the Raman transition in the frequency domain can be several times smaller than the frequency interval $\Delta\omega_{\text{effR}}$, when the Raman pulse duration τ is long enough. A theoretical RS of quasi-Bragg diffraction up to second order with a detecting Raman pulse duration of $100 \mu\text{s}$ is shown in Fig. 1(d). It shows that adjacent momentum states can be clearly resolved in the frequency domain. With this method, the final superposition states can be identified without requiring a long flight time any more, and their respective populations can be obtained from RS.

III. EXPERIMENTS

A. The laser system

Extra Raman beams are required for the present detection technique. Figure 2(a) shows a schematic of the laser system, based on a frequency-doubled technique, used to drive both the Bragg transitions and the Raman transitions with a single laser source. The 1560-nm seed laser injects an Er-doped fiber amplifier with a peak emission power of 30 W. The output beam from the Er-doped fiber amplifier is then frequency doubled through a periodically poled magnesium-oxide-doped lithium niobate (PPMgO:LN) crystal and stabilized with a red detuning of 3.2 GHz to the $|F = 1\rangle \rightarrow |F' = 2\rangle$ transition in the ^{87}Rb D_2 line. Going through the same optical path, the Bragg beams and the Raman beams can be realized, respectively, by choosing whether or not to modulate the frequency of the seed laser. Bragg beams require a small frequency

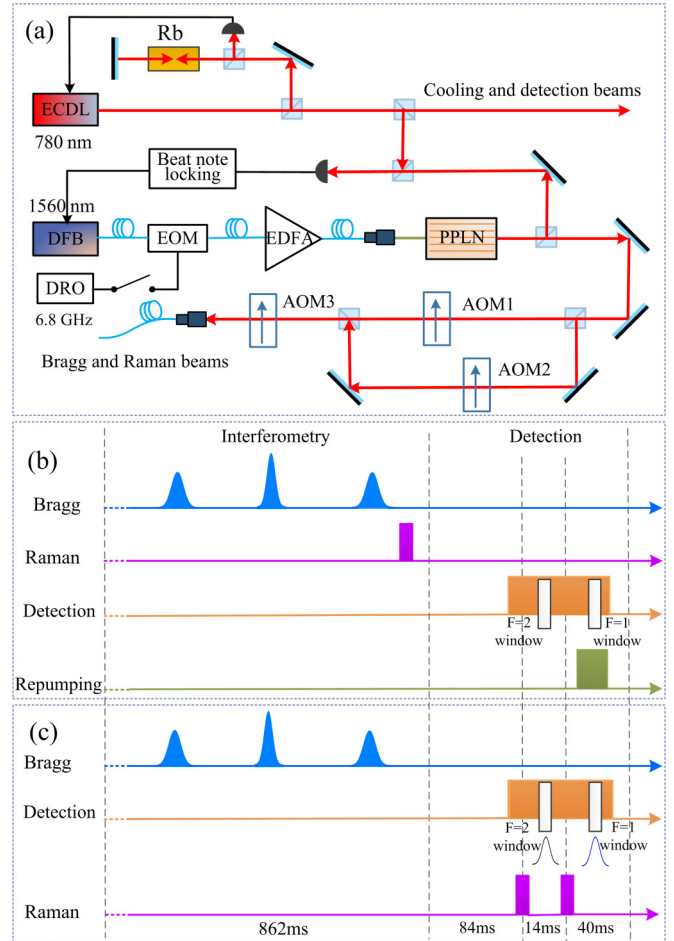


FIG. 2. (a) Optics of the Raman beams and Bragg beams. An external cavity diode laser (ECDL) at 780 nm is locked to the $|F = 2\rangle \rightarrow |F' = 3\rangle$ transition in the ^{87}Rb D_2 line. The ECDL is then used as a frequency reference to lock the frequency of distributed feedback (DFB) laser at 1560 nm. Finally, the doubled frequency of the DFB laser is stabilized with a red detuning of 3.2 GHz to the $|F = 1\rangle \rightarrow |F' = 2\rangle$ transition in the ^{87}Rb D_2 line. The Raman beams are generated by adding sidebands on the seed laser with an electro-optic modulator (EOM) driven by a dielectric resonator oscillator (DRO) operating at 6.8 GHz. The Bragg beams require a small frequency difference between the two light fields; this is realized by two acousto-optic modulators (AOM1 and AOM2). A third, AOM3, shapes the Bragg pulses with a Gaussian amplitude profile and the Raman pulses with a square-wave amplitude profile. (b) Experimental time sequence for Raman spectroscopy detection with multiple launches (RSML). Complete RS requires multiple launches, and the whole time used for a single run is 1 s. (c) Experimental time sequence for Raman spectroscopy detection with a single launch (RSSL). The delay time between the two Raman pulses is about 14 ms.

difference between the two light fields; it is realized by two acousto-optic modulators (AOM1 and AOM2, respectively) with perpendicular polarizations. Raman beams are generated by adding sidebands with an electro-optic modulator driven by a dielectric resonator oscillator operating at 6.8 GHz. Simultaneously, the AOM2 is closed to avoid the effect of multiple frequencies. With this Raman-beam scheme, one can

ensure a high power and avoid the problem of phase noise due to variations of optical paths. Compared to the usual method of using at least two lasers for those frequency components [26], this compact scheme for high-power Bragg beams and low-phase-noise Raman beams uses only a single laser source.

B. Atom interferometry

The Bragg atom interferometer is based on interfering ensembles of ^{87}Rb atoms in an atomic fountain configuration [3]. Initially, about 10^9 atoms are trapped within 200 ms in a three-dimensional magneto-optical trap (3D-MOT) from the intense beam of a 2D-MOT. The trapped atoms are then further cooled down in a moving optical molasses to a temperature of $9\ \mu\text{K}$. When the atoms arise to the detection region, a combination of microwave and optical Raman pulses is applied to prepare about 10^6 atoms in the magnetic-field-insensitive state $|F = 1, m_F = 0\rangle$ with a typical vertical velocity spread of about $0.3v_r$. Once the atoms are prepared with a narrow velocity spread, the sample is ready for interferometry using Bragg diffraction.

The resonance condition for Bragg diffraction is $\delta_B = \omega_0 + 4n\omega_r$, where ω_0 is the Doppler frequency shift due to free fall, ω_r is the single-photon recoil frequency, and n is the order of diffraction. In order to maximize the diffraction efficiency, the Bragg pulses are shaped into a Gaussian amplitude profile by controlling the radio-frequency power of the AOM3 driver. The Bragg beams and Raman beams reach the vacuum chamber via a polarization-maintaining fiber and are collimated at a $1/e^2$ intensity diameter of 18 mm. For four-photon Bragg transitions, each Bragg beam has a peak power of 200 mW and a π pulse duration of $\sigma_\tau = 15\ \mu\text{s}$. In particular, to decrease the power instability and increase the long-term stability of gravity measurements, the power of each Bragg beam is locked separately. To suppress the residual vibration noise of the Bragg mirror, an ultralow-noise active vibration isolator system is employed in our apparatus [3].

When the atoms reach the elongated magnetically shielded interferometry region, we constructed a Mach-Zehnder interferometer by applying the $\pi/2$ - π - $\pi/2$ sequence of three Bragg pulses. The interference phase $\Delta\Phi$ is connected to the local gravitational acceleration g by $\Delta\Phi = n(k_{\text{effB}}g - \alpha)T^2$, where k_{effB} is the effective wave vector of Bragg transitions, α is the sweeping rate, and T is the time of free evolution between pulses. Since the interference phase $\Delta\Phi$ is proportional to n , the resolution of g measurements can be increased with n .

To measure the population of the interferometer's output states independently, the RS detection method is used to detect the falling atoms, on the basis of two-state sequential detection [33]. Previously, all atoms were populated in state $|F = 1\rangle$. Once the interference finishes, the detecting Raman pulse with a frequency ω_{effR} is switched on. Then the selected atoms at a specific velocity are imaged in state $|F = 2\rangle$, and their transition probability is obtained by the normalized detection method. Finally, the RS of atomic distribution is obtained by sequentially scanning the effective Raman frequency ω_{effR} . In this way, a complete RS detection requires multiple launches, and the time sequence of RS detection with multiple launches (RSML) is shown in Fig. 2(b). The

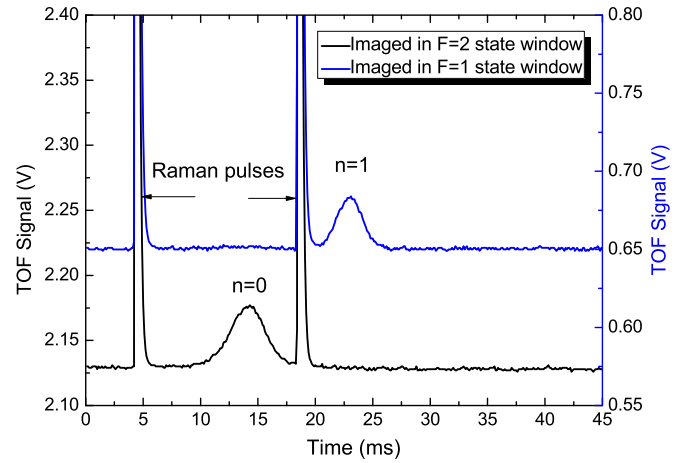


FIG. 3. Typical TOF signals of the first-order interferometer using RSSL detection.

population of final states $|p\rangle$ and $|p - 2n\hbar k\rangle$ can be obtained by integrating the atomic distribution in RS. This RS technique provides a tool for momentum-resolved detection. Still, the low sampling rate due to the RSML method limits the bandwidth and sensitivity of our system.

In order not to reduce the sampling rate, a scheme of RS detection with a single launch (RSSL) is designed for the two output states, whose corresponding time sequence is shown in Fig. 2(c). Here, a first-order interferometer is taken as our example. When the output states fall back to the detection region, the detection beam resonant with the transition of $|F = 2\rangle \rightarrow |F' = 3\rangle$ is switched on. The $n = 0$ order atoms are then imaged in the $|F = 2\rangle$ state window by the first detecting Raman pulse, which has an optimal Raman resonance frequency for $n = 0$ order atoms and pumps the $n = 0$ order atoms from the $|F = 1\rangle$ to the $|F = 2\rangle$ state. Similarly, the $n = 1$ order atoms are correspondingly imaged in the $|F = 1\rangle$ state window by the second detecting Raman pulse. Typical TOF signals with RSSL detection are shown in Fig. 3. In this way, the interferometer's output states are separately imaged in a single passing detection region. Compared to traditional TOF detection, RSSL detection does not reduce the sampling rate and helpfully selects more purity clouds for detection. Moreover, the repumping beam is no longer needed in this detection scheme.

IV. RESULTS AND DISCUSSION

A. The contrast

The contrast of the interferometer is mainly dependent on the efficiency of the Bragg mirrors and beam splitters. In the quasi-Bragg regime, we set the pulse's amplitude and duration appropriately to optimize the efficiency of Bragg transitions. Direct measurement of the momentum distribution of the first-order Bragg diffraction has been performed using the RSML method, and the adjacent momentum states in the frequency domain are completely separated as shown in Fig. 4(a). By integrating the atomic distribution, a π pulse efficiency of 88% and a $\pi/2$ pulse efficiency of 50% are achieved for first-order Bragg diffraction.

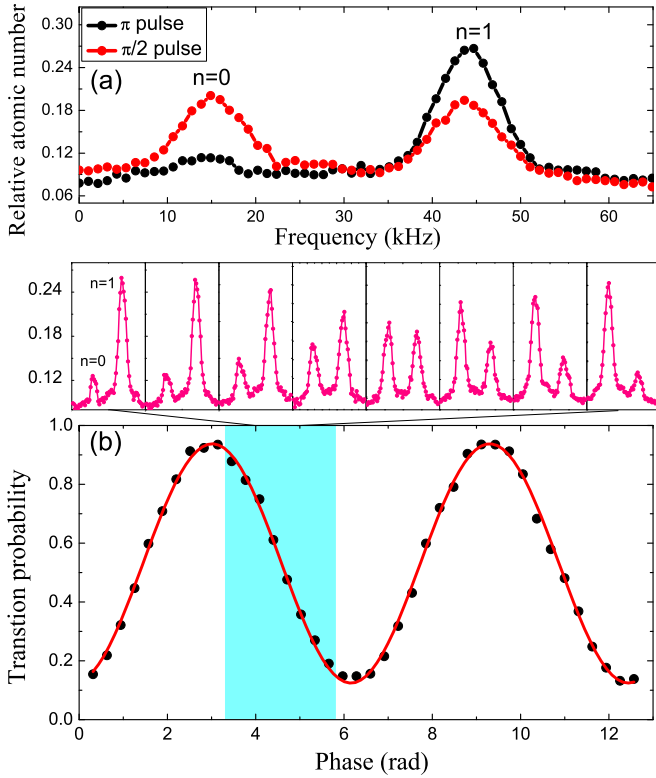


FIG. 4. (a) RS curves of Bragg transitions with $n = 1$, which represent the atomic distribution of the Bragg $\pi/2$ pulse (red curve) and π pulse (black curve). (b) Typical Bragg atom interferometer fringes (black points) for $n = 1$ at $T = 1$ ms. The solid red line is a least-squares sinusoidal fitting to the experimental data. One fringe consists of 40 points, and every point is obtained from the Raman spectroscopy as the shaded region in the fringe.

Because of the high efficiency of low-order Bragg transitions, most experiments have observed a high fringe contrast [34–36]. Using the RSML method, we perform the interference experiment by applying the $\pi/2$ - π - $\pi/2$ sequence of three Bragg pulses. Figure 4(b) shows the high visibility of 81% for $n = 1$ at $T = 1$ ms, approaching the case of a Bose-Einstein condensate source [37]. The high diffraction efficiency and efficient RS detection contribute to this high visibility. The least-squares sine fitting of the fringe gives an uncertainty of 8 mrad, indicating that this detection method can be applied to some precision measurements.

In the Bragg atom interferometer, to increase the sensitivity, it is imperative to maintain a high fringe visibility at a large value of T . However, there are many factors contributing to the loss of fringe visibility at a long interrogation time T , such as thermal expansion, wavefront distortions of the Bragg beams, and the tilt of the fountain. In addition, when the Raman pulse duration for RS detection is not large enough, the neighboring momentum states will be detected simultaneously, and the corresponding fringe contrast will be reduced. In this subsection, we study the fringe contrast theoretically and experimentally as a function of the detecting Raman pulse duration τ . In particular, we analyze the dependence of the fringe visibility on the interrogation time T using RS detection, compared with traditional TOF detection.

The velocity distribution of atoms in momentum state $|p - 2n\hbar k\rangle$ is a Gaussian lineshape as

$$g_n = \frac{1}{\sqrt{2\pi}\sigma_v} e^{-\frac{[v-(v_d-2nv_r)]^2}{2\sigma_v^2}}, \quad (8)$$

where $v_d - 2nv_r$ is the center of the velocity family distribution and σ_v is its width. Initially, the ensemble is in the $|F = 1\rangle$ state. After a Raman pulse, the pulse-dependent probabilities $P_{F=2}(\tau)$ of occupying the internal states $|F = 2\rangle$ are after Ref. [31],

$$P_{F=2}(\tau) = \frac{|\Omega_1|^2|\Omega_2|^2}{4\bar{\Omega}^2\Delta^2} \sin^2\left(\frac{\bar{\Omega}\tau}{2}\right), \quad (9)$$

where Ω_1 and Ω_2 are the single-photon Rabi frequencies of the two Raman beams, respectively, and $\bar{\Omega}$ is the two-photon Rabi frequency driven by a Raman pair. Here, the Raman frequency ω_{effR} ($\omega_{\text{effR}} = 2\pi f$) is introduced by the two-photon Rabi frequency $\bar{\Omega}$ and can be written as

$$\bar{\Omega}^2 = \left(\frac{|\Omega_1|^2}{4\Delta} - \frac{|\Omega_2|^2}{4\Delta} - \delta\right)^2 + \frac{|\Omega_1|^2|\Omega_2|^2}{4\Delta^2}, \quad (10)$$

$$\delta = \omega_{\text{effR}} - (\omega_{ba} + k_{\text{effR}}v + k_{\text{effR}}v_r).$$

Considering the atomic velocity distribution g_n , the lineshape of the RS for the momentum state $|p - 2n\hbar k\rangle$ can be written as

$$g'_n(f) = \int_{-\infty}^{+\infty} P_{F=2}(\tau)g_nv dv$$

$$= \int_{-\infty}^{+\infty} \frac{|\Omega_1|^2|\Omega_2|^2}{4\bar{\Omega}^2\Delta^2} \sin^2\left(\frac{\bar{\Omega}\tau}{2}\right) \frac{1}{\sqrt{2\pi}\sigma_v} e^{-\frac{[v-(v_0-2nv_r)]^2}{2\sigma_v^2}} dv. \quad (11)$$

The population of n th-order atoms can be calculated by

$$P_n = \int_{f_n-\sigma}^{f_n+\sigma} g'_n(f)df, \quad (12)$$

where f_n is the resonance frequency of n th-order atoms, and a 2σ frequency width of RS covers most the atoms. For quasi-Bragg diffraction, the normalized populations P_0 and P_n , respectively, denote the atomic population of the orders of 0 and n . In fact, besides the detected atoms of the target states, there are some mixed adjacent-state resonant atoms due to the short Raman pulse duration used in detection, which decreases the contrast. Here, we take $n = 0$ order atoms, for example. After a pulse duration τ , the populations of $n = 0$ order atoms in RS are

$$P'_0 = \int_{f_0-\sigma}^{f_0+\sigma} (g'_0(f) + g'_{\pm 1}(f) + \dots g'_{\pm n}(f))df. \quad (13)$$

For the n th-order Bragg process, the contrast C can be given as the difference between maximum and minimum normalized populations when observing $n = 0$ order atoms:

$$C = \frac{P_{0\text{max}} - P_{0\text{min}}}{P_{0\text{max}} + P_{0\text{min}}}. \quad (14)$$

Considering that atoms in momentum states for $n = \pm 2$ are less involved in interference, we mainly consider the effect of

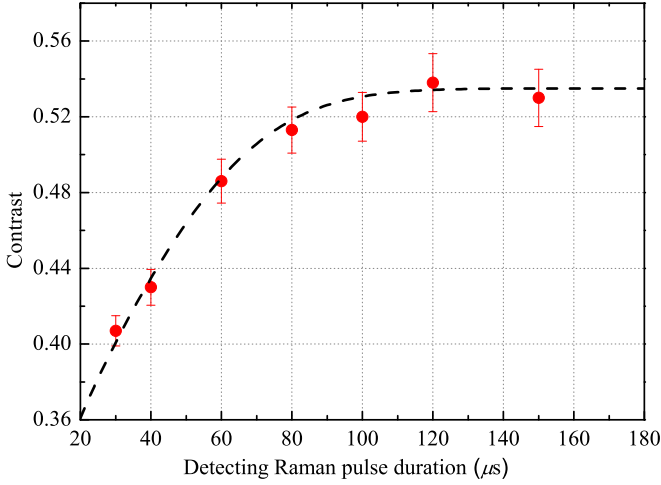


FIG. 5. Comparison between the theoretical simulation and the experimental data for the fringe contrast.

$n = \pm 1$ order atoms and treat them as the background atoms. Therefore, the contrast of the RS detection is calculated via the expression

$$C_{\text{det}} = \frac{C}{1 + 2AP_{+1} + 2BP_{-1}}, \quad (15)$$

where A and B are coefficients proportional to the number of $n = +1$ and $n = -1$ order atoms. Figure 5 shows experimental data (red circles) illustrating the fringe contrast C_{det} as a function of the detecting Raman pulse duration τ . The fringe contrast is observed with $n = 2$ at an interrogation time of $T = 60$ ms. Using Eqs. (11)–(15) and a rough estimate of the frequency width ($\sigma = 1/\tau$), the simulation results shown in Fig. 5 (dashed black curve) agree well with the experimental results. The fringe contrast increases rapidly with increasing Raman pulse duration τ in detection, until the duration is more than $100 \mu\text{s}$, at which the contrast does not increase due to the lower number of overlapped atoms in the RS.

In order to maximize the visibility, a $100\text{-}\mu\text{s}$ detecting Raman pulse is selected for the Bragg atom interferometer. Figure 6 shows the fringe visibility for first and second Bragg order as a function of the interrogation time T using RS detection, compared with traditional TOF detection. Benefiting from the momentum-resolved detection, the visibility obtained with RS detection is significantly higher than that with TOF detection. At a visibility of 10%, we have achieved a Bragg atom interferometer with the long interrogation time of up to $T = 250$ ms for $n = 1$ and $T = 180$ ms for $n = 2$, which provides an important guarantee for high-sensitivity Bragg atom interferometry. In our apparatus, the fringe visibility at a short interrogation time is mainly limited by the efficiency of the π pulse, and at a long interrogation time is mainly limited by the thermal expansion of the atomic cloud.

B. The sensitivity

In multiphoton Bragg diffraction, the sensitivity of the interferometer is proportional to nT^2 . Therefore, we struggle to achieve high-precision measurements both with a high-

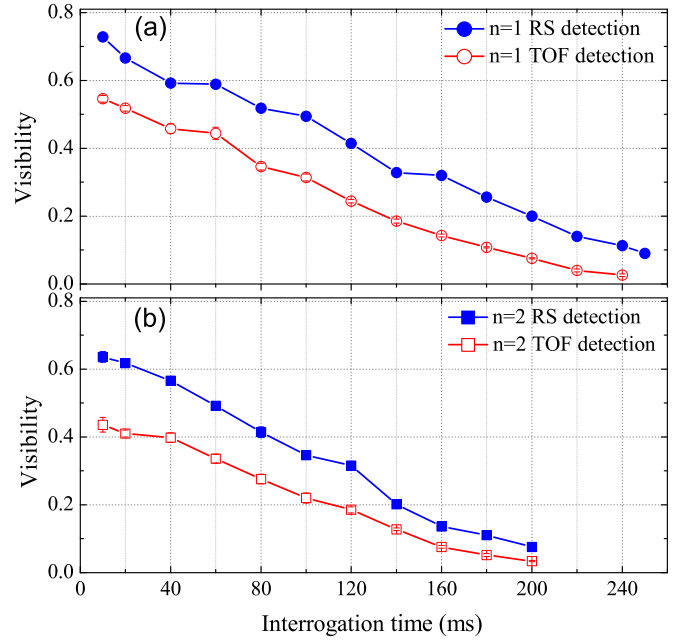


FIG. 6. (a) First-order fringe visibility for RS detection and TOF detection (filled and open blue circles, respectively) as a function of the interrogation time T . (b) Second-order fringe visibility for RS detection and TOF detection (filled and open blue squares, respectively) as a function of the interrogation time T . The visibility obtained with RS detection is higher than that with TOF detection. Due to the limitation of the pulse efficiency, the interferometer with $n = 1$ has a higher visibility and longer interrogation time T than the one with $n = 2$.

order n and with a long interrogation time T . Constrained by the atomic source's momentum distribution, we have attained a π pulse efficiency of 81% with $n = 2$ and the long interrogation time of $T = 180$ ms with a fringe visibility of about 10%–15%. By recording the long-term interferometer phase using RSSL detection, a sensitivity of up to $\Delta g/g = 4.0 \times 10^{-8}/\sqrt{\text{Hz}}$ is achieved. For the Bragg atom interferometer, it should be noted that while the estimated phase noise is proportional to n , the sensitivity of the interferometer does not depend on n . In fact, we have achieved a $T = 250$ ms, $n = 1$ interferometer, which possesses nearly the same accumulated phase as the $T = 180$ ms, $n = 2$ interferometer but has a smaller phase noise contribution for the sensitivity. Using the fringe-locked method, we achieved a continuous g measurement over 22 h as shown in Fig. 7(a). This figure shows that the experimental data with a 60-s averaging period (blue points) are consistent with the theoretical model of solid Earth tide (red curve), indicating that the Bragg atom interferometer using RSSL detection is robust in continuous measurements. The residual of the experimental data and tidal model is shown in Fig. 7(b). The Allan standard deviation of the residual acceleration is shown in Fig. 7(c). It shows that this device has achieved a gravitational acceleration sensitivity of $\Delta g/g = 1.9 \times 10^{-8}/\sqrt{\text{Hz}}$. After an integration time of 1000 s, the resolution of $7 \times 10^{-10}g$ can be achieved. By comparison, using traditional TOF detection we have only achieved a maximum interrogation time $T = 200$ ms for the

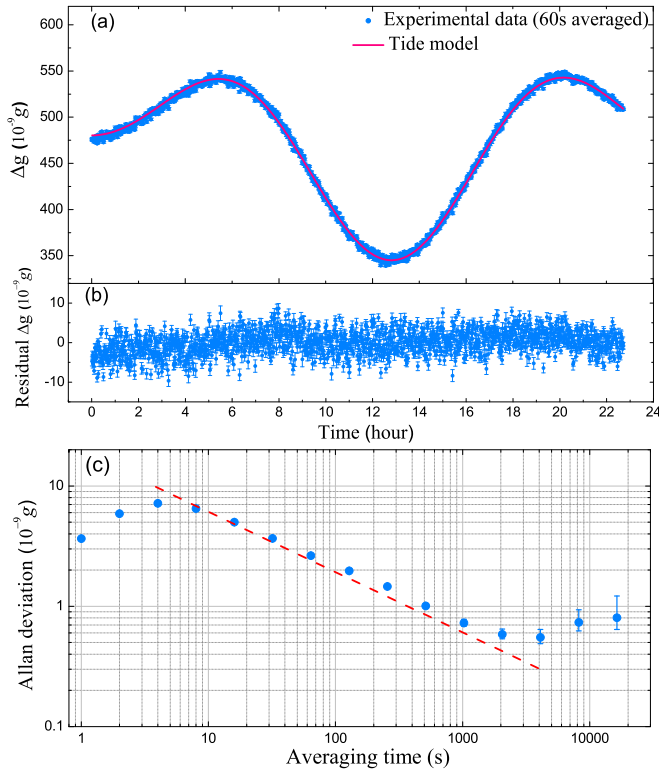


FIG. 7. (a) Continuous gravity measurements of more than 22 h operated by our gravimeter on 23 August 2017. Each data point (blue point) represents an average of 60 individual measurements in 60 s. The red curve is the theoretical model of solid Earth tide. (b) Residual of the experimental data and the solid Earth tide theory. (c) Allan deviation of the g measurement.

first-order interferometer, with a gravitational acceleration sensitivity of $\Delta g/g = 3.2 \times 10^{-8} / \sqrt{\text{Hz}}$.

We have demonstrated a Bragg atom interferometer with a high fringe visibility and sensitivity by using the RS detection method and solved the detection problem of overlapped output states. However, with an increase in the diffraction order n , the maximum diffraction efficiency and interrogation time T decrease, and the corresponding detection noise increases. We attribute this consequence to the transverse momentum spread of the atomic source. In future work, we expect to improve the diffraction order by reducing the transverse momentum spread of the samples.

C. The noise of RSSL detection

A detection system with a high SNR is required in a precision atom interferometer. The detection noise consists of three main parts [17,33]: the quantum projection noise $\sigma_{P(\text{QPN})}$, the electronic noise of the photodiodes $\sigma_{P(\text{EN})}$, and the contribution of the frequency and intensity noise of detection beams $\sigma_{P(\text{DN})}$. The quantum projection noise $\sigma_{P(\text{QPN})}$ and the electronic noise $\sigma_{P(\text{EN})}$ are related to the number of detected atoms. In our experiment, about 10^5 atoms fall back to the detection region after the interference. For the traditional TOF detection method, $\sigma_{P(\text{QPN})}$, $\sigma_{P(\text{EN})}$, and $\sigma_{P(\text{DN})}$ are measured to be 0.16%, 0.21%, and 0.18%, respectively.

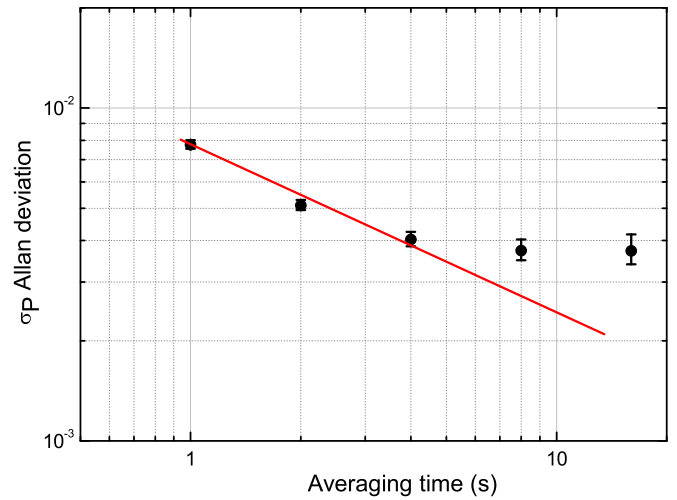


FIG. 8. Allan standard deviation of the transition probability σ_P for RSSL detection.

For the typical RSSL detection, when the atoms fall back to the detection region, two Raman π pulses are used to select the atoms of $n = 0$ and $n = 1$ order, respectively. In the selection, atoms in state $|F = 1\rangle$ are pumped to state $|F = 2\rangle$ by the Raman beams. The efficiency of Raman transitions is about $\eta = 30\%$, which further reduces the actual number of atoms detected for each state. In this case, we estimate that $\sigma_{P(\text{QPN})}$ and $\sigma_{P(\text{EN})}$ are limited to 0.29% and 0.7% for 3×10^4 atoms, respectively, and $\sigma_{P(\text{DN})}$ remains the same at 0.18%.

In addition, the fluctuations in transition probability between the two detecting Raman pulses also contribute to the detection noise and can be calculated by

$$\Delta P = P_1^i - P_1^{i+1} \approx P_1(1 - P_1) \frac{\Delta\eta}{\eta}, \quad (16)$$

where P_1^i is the i th measurement of the Bragg transition probability for $n = 1$ order, and $\Delta\eta$ is the transition probability's fluctuations in the Raman pulses between two adjacent launches. According to Eq. (9), we get that the fluctuations in transition probability $\Delta\eta$ are mainly composed of three parts: the fluctuations in the Raman pulse duration, the intensity noise of Raman beams, and the frequency noise of Raman beams. From the measurement of these three noise sources of Raman beams, $\Delta\eta$ is determined to be 0.16%, which induces a detection noise of $\Delta P = 0.13\%$.

In total, the estimative detection noise of RSSL detection is 0.79%. We have also measured the detection noise with the method referred to in [39]. Figure 8 shows the measured Allan standard deviation of the transition probability σ_P , giving $\sigma_P = 0.76\%$ in 1 s, which is close to the expected detection noise. The resulting observed SNR for RSSL detection is 130:1 in 1 s. (The SNR is given by $\text{SNR} = 1/\sigma_P$, in Ref. [38].)

The variances of the interference phase are related to the standard deviation σ_P by the formula $\sigma_\phi = 2\sigma_P/C$, with C the contrast of the interferometer. Considering a typical contrast of 9% for the $T = 250$ ms, $n = 1$ interferometer, a detection noise of 169 mrad/ $\sqrt{\text{Hz}}$ can be obtained, corresponding to an acceleration sensitivity of $1.7 \times 10^{-8} g/\sqrt{\text{Hz}}$, which sets the actual limit on our interferometer sensitivity.

Another important contribution to the interferometer noise is the laser phase noise of the passive Bragg laser system. Usually, we use the sensitivity function [25,39] to calculate the contribution of the interferometer phase noise. With the sensitivity function and the power spectral density of phase noise of the Bragg beams, the contribution to the interferometer phase noise is calculated as $149 \text{ mrad}/\sqrt{\text{Hz}}$, corresponding to an acceleration sensitivity of $1.5 \times 10^{-8} g/\sqrt{\text{Hz}}$.

V. CONCLUSION AND OUTLOOK

We have presented a simple and practical detection method based on RS for a Bragg atom interferometer. With this method, the interferometer's output states are imaged in a narrow frequency domain, which not only improves the fringe visibility but also avoids multistate effects in the interferometer phase. With these advantages, we have demonstrated a short-term sensitivity of $\Delta g/g = 1.9 \times 10^{-8}/\sqrt{\text{Hz}}$ in a Bragg-type atom gravimeter. For an integration time of 1000 s, the resolution reaches $7 \times 10^{-10} g$. This resolution is currently limited by the detection noise and the laser phase noise.

In recent years, significant efforts have been made to develop a compact system that incorporates ultracold atomic ensembles as a portable sensing device [40,41]. Using the technique of large-momentum-transfer beam splitting in the small-volume apparatus will be a significant advantage, and this momentum-resolved detection demonstrates a proven and ultrastable detection technique that does not require a space separation for the atomic cloud. Similarly, this detection method also allows improved detection of atom interferometry based on Bragg transitions in an optical cavity with a compact size and low power [42,43]. In addition, this detection method can be used in fundamental physics experiments such as detection of gravitational waves [44] and tests of the Einstein equivalence principle [45].

ACKNOWLEDGMENT

This work was supported by the National Natural Science Foundation of China (Grants No. 91636219, No. 11625417, No. 11727809, No. 11474115, and No. 91736311).

-
- [1] A. Peters, K. Y. Chung, and S. Chu, *Nature* **400**, 849 (1999).
 - [2] A. Louchet-Chauvet, T. Farah, Q. Bodart, A. Clairon, A. Landragin, S. Merlet, and F. Pereira Dos Santos, *New J. Phys.* **13**, 065025 (2011).
 - [3] Z. K. Hu, B. L. Sun, X. C. Duan, M. K. Zhou, L. L. Chen, S. Zhan, Q. Z. Zhang, and J. Luo, *Phys. Rev. A* **88**, 043610 (2013).
 - [4] M. J. Snadden, J. M. McGuirk, P. Bouyer, K. G. Haritos, and M. A. Kasevich, *Phys. Rev. Lett.* **81**, 971 (1998).
 - [5] I. Dutta, D. Savoie, B. Fang, B. Venon, C. L. Garrido Alzar, R. Geiger, and A. Landragin, *Phys. Rev. Lett.* **116**, 183003 (2016).
 - [6] R. Bouchendira, P. Cladé, S. Guellati-Khélifa, F. Nez, and F. Biraben, *Phys. Rev. Lett.* **106**, 080801 (2011).
 - [7] G. Rosi, F. Sorrentino, L. Cacciapuoti, M. Prevedelli, and G. M. Tino, *Nature* **510**, 518 (2014).
 - [8] M. K. Zhou, Z. K. Hu, X. C. Duan, B. L. Sun, J. B. Zhao, and J. Luo, *Phys. Rev. A* **82**, 061602(R) (2010).
 - [9] S. Fray, C. A. Diez, T. W. Hänsch, and M. Weitz, *Phys. Rev. Lett.* **93**, 240404 (2004).
 - [10] X. C. Duan, X. B. Deng, M. K. Zhou, K. Zhang, W. J. Xu, F. Xiong, Y. Y. Xu, C. G. Shao, J. Luo, and Z. K. Hu, *Phys. Rev. Lett.* **117**, 023001 (2016).
 - [11] L. Zhou, S. T. Long, B. Tang, X. Chen, F. Gao, W. C. Peng, W. T. Duan, J. Q. Zhong, Z. Y. Xiong, J. Wang, Y. Z. Zhang, and M. S. Zhan, *Phys. Rev. Lett.* **115**, 013004 (2015).
 - [12] P. Hamilton, M. Jaffe, P. Haslinger, Q. Simmons, H. Müller, and J. Khoury, *Science* **349**, 849 (2015).
 - [13] K.-Y. Chung, S.-W. Chiow, S. Herrmann, S. Chu, and H. Müller, *Phys. Rev. D* **80**, 016002 (2009).
 - [14] I. Serre, L. Pruvost, and H. T. Duong, *Appl. Opt.* **37**, 1016 (1998).
 - [15] W. Ketterle, D. S. Durfee, and D. M. Stamper-Kurn, [arXiv:cond-mat/9904034v2](https://arxiv.org/abs/cond-mat/9904034v2).
 - [16] C. E. Simien, Y. C. Chen, P. Gupta, S. Laha, Y. N. Martinez, P. G. Mickelson, S. B. Nagel, and T. C. Killian, *Phys. Rev. Lett.* **92**, 143001 (2004).
 - [17] G. Santarelli, Ph. Laurent, P. Lemonde, A. Clairon, A. G. Mann, S. Chang, A. N. Luiten, and C. Salomon, *Phys. Rev. Lett.* **82**, 4619 (1999).
 - [18] G. W. Biedermann, X. Wu, L. Deslauriers, K. Takase, and M. A. Kasevich, *Opt. Lett.* **34**, 347 (2009).
 - [19] K. S. Hardman, P. B. Wigley, P. J. Everitt, P. Manju, C. C. N. Kuhn, and N. P. Robins, *Opt. Lett.* **41**, 2505 (2016).
 - [20] F. K. Fatemi, M. L. Terraciano, M. Bashkansky, and Z. Dutton, *Opt. Express* **17**, 12971 (2009).
 - [21] M. Lee, J. H. Han, J. H. Kang, M. S. Kim, and Y. Shin, *Phys. Rev. A* **95**, 043627 (2017).
 - [22] H. Müller, S.-W. Chiow, Q. Long, S. Herrmann, and S. Chu, *Phys. Rev. Lett.* **100**, 180405 (2008).
 - [23] S.-W. Chiow, T. Kovachy, H. C. Chien, and M. A. Kasevich, *Phys. Rev. Lett.* **107**, 130403 (2011).
 - [24] P. A. Altin, M. T. Johnsson, V. Negnevitsky, G. R. Dennis, R. P. Anderson, J. E. Debs, S. S. Szigeti, K. S. Hardman, S. Bennetts, G. D. McDonald, L. D. Turner, J. D. Close, and N. P. Robins, *New J. Phys.* **15**, 023009 (2013).
 - [25] T. Mazzoni, X. Zhang, R. D. Aguila, L. Salvi, N. Poli, and G. M. Tino, *Phys. Rev. A* **92**, 053619 (2015).
 - [26] G. D'Amico, F. Borselli, L. Cacciapuoti, M. Prevedelli, G. Rosi, F. Sorrentino, and G. M. Tino, *Phys. Rev. A* **93**, 063628 (2016).
 - [27] B. V. Estey, Ph.D. thesis, University of California, Berkeley 2016.
 - [28] R. H. Parker, C. H. Yu, B. Estey, W. C. Zhong, E. Huang, and H. Müller, *Phys. Rev. A* **94**, 053618 (2016).
 - [29] Y. Cheng, K. Zhang, L. L. Chen, W. J. Xu, Q. Luo, M. K. Zhou, and Z. K. Hu, *AIP Adv.* **7**, 095211 (2017).

- [30] M. Kasevich, D. S. Weiss, E. Riis, K. Moler, S. Kasapi, and S. Chu, *Phys. Rev. Lett.* **66**, 2297 (1991).
- [31] K. Moler, D. S. Weiss, M. Kasevich, and S. Chu, *Phys. Rev. A* **45**, 342 (1992).
- [32] H. Müller, S.-W. Chiow, and S. Chu, *Phys. Rev. A* **77**, 023609 (2008).
- [33] A. Gauguier, B. Canuel, T. Lévêque, W. Chaibi, and A. Landragin, *Phys. Rev. A* **80**, 063604 (2009).
- [34] D. E. Miller, J. R. Anglin, J. R. Abo-Shaeer, K. Xu, J. K. Chin, and W. Ketterle, *Phys. Rev. A* **71**, 043615 (2005).
- [35] Y. Torii, Y. Suzuki, M. Kozuma, T. Sugiura, T. Kuga, L. Deng, and E. W. Hagley, *Phys. Rev. A* **61**, 041602(R) (2000).
- [36] K. S. Hardman, C. C. N. Kuhn, G. D. McDonald, J. E. Debs, S. Bennetts, J. D. Close, and N. P. Robins, *Phys. Rev. A* **89**, 023626 (2014).
- [37] J. E. Debs, P. A. Altin, T. H. Barter, D. Döring, G. R. Dennis, G. McDonald, R. P. Anderson, J. D. Close, and N. P. Robins, *Phys. Rev. A* **84**, 033610 (2011).
- [38] S. Bize, P. Laurent, M. Abgrall, H. Marion, I. Maksimovic, L. Cacciapuoti, J. Grünert, C. Vian, F. Pereira Dos Santos, P. Rosenbusch, P. Lemonde, G. Santarelli, P. Wolf, A. Clairon, A. Luiten, M. Tobar, and C. Salomon, *J. Phys. B* **38**, S449 (2005).
- [39] J. L. Göüet, T. Mehlstäubler, J. Kim, S. Merlet, A. Clairon, A. Landragin, and F. Pereira Dos Santos, *Appl. Phys. B*, **92**, 133 (2008).
- [40] A. Hinton, M. Perea-Ortiz, J. Winch *et al.*, *Philos. Trans. R. Soc. A* **375**, 20160238 (2017).
- [41] J. P. McGilligan, P. F. Griffin, R. Elvin, S. J. Ingleby, E. Riis, and A. S. Arnold, *Sci. Rep.* **7**, 384 (2017).
- [42] P. Hamilton, M. Jaffe, J. M. Brown, L. Maisenbacher, B. Estey, and H. Müller, *Phys. Rev. Lett.* **114**, 100405 (2015).
- [43] M. Dovale-Álvarez, D. D. Brown, A. W. Jones, C. M. Mow-Lowry, H. Miao, and A. Freise, *Phys. Rev. A* **96**, 053820 (2017).
- [44] M. A. Norcia, J. R. K. Cline, and J. K. Thompson, *Phys. Rev. A* **96**, 042118 (2017).
- [45] G. Rosi, G. D'Amico, L. Cacciapuoti, F. Sorrentino, M. Prevedelli, M. Zych, Č. Brukner, and G. M. Tino, *Nat. Commun.* **8**, 15529 (2017).